Pre-flight and In-flight Calibration and Performance of the Terminal Tracking Cameras (TTCams) on the NASA Lucy Mission

Y. Zhao[1], J.F. Bell III[1], E. Sahr[2], E. Lessac-Chenen[2], C. Adam[2], E. Cisneros[1], A. Winhold[1], M. Caplinger[3], M. Ravine[3], J. Schaffner[3], J. Shamah[3], S. Mottola[4]

[1]Arizona State Univ., School of Earth and Space Exploration, Tempe, AZ
[2]KinetX Inc., Tempe, AZ
[3]Malin Space Science Systems, Inc., San Diego, CA
[4]Institute for Planetary Research, DLR, Berlin, Germany

Key Points:

- We detail the pre-flight and initial in-flight characterization and calibration of the NASA Lucy mission's Terminal Tracking Camera system.
- Pre-flight results primarily include sensor and system characterization (gain, dark current, linearity, flat field, radiometry, bad pixels).
- We describe the calibration pipeline as well as initial in-flight optical assessment and radiometry results from Earth, Moon, and star field imaging.

Corresponding author: Y. Zhao, amyzhao@asu.edu

Abstract

The Terminal Tracking Camera (TTCam) imaging system on the NASA Lucy Discovery mission consists of a pair of cameras that will be used mainly as a navigation and target acquisition system for the mission's asteroid encounters. However, a secondary science-focused function of the TTCam system is to provide wide-angle broadband images over a large range of phase angles around close approach during each asteroid flyby. The scientific data acquired by TTCam can be used for shape modeling and topographic and geologic analyses. This paper describes the pre-flight and initial in-flight calibration and characterization of the TTCams, including the development of a radiometric calibration pipeline to convert raw TTCam images into radiance and radiance factor (I/F) images, along with their uncertainties. Details are also provided here on the specific calibration algorithms, the origin and archived location of the required ancillary calibration files, and the archived sources of the raw calibration and flight data used in this analysis.

1 Introduction

The Trojan asteroids of Jupiter are a large population of relatively small, relatively low albedo asteroids that orbit the Sun in two distinct "clouds" of small bodies centered near the stable Jupiter-Sun L4 and L5 Lagrange points some 60° ahead of and behind Jupiter itself. Studying the Trojans provides an opportunity to learn more about the history and formation of the solar system, including the possible origins of organic materials that ultimately led to the development of life on Earth (e.g., Levison et al., 2021). The NASA Lucy Trojan asteroid Discovery mission is the first mission to explore the Trojans up close. Lucy was launched in October 2021 and between 2023 and 2033 the mission will nominally conduct flybys of two main belt asteroids and five different Trojan systems consisting of at least eight different asteroids, because some of those systems are binaries or have satellites. Details about the Lucy mission science goals, mission profile, and instrument suite can be found in Levison et al. (2021) and Olkin et al. (2021).

One of the instrument systems on Lucy is called the Terminal Tracking Camera (TTCam; Bell et al. (2023)), which consists of a pair of identical digital cameras (for block redundancy) and an associated Digital Video Recorder (DVR) electronics control/power supply electronics for each, located on the spacecraft's Instrument Pointing Platform (IPP). Only one camera is intended to be used at a time. The primary camera, intended for nominal use during the mission, is referred to as TTCam1 (connected to DVR1, serial number 194503) and the secondary or backup camera is referred to as TTCam2 (connected to DVR2, serial number 194504). Figure 1 shows both TTCam1 and TTCam2 on the Lucy spacecraft.

The TTCams are primarily designed to perform a guidance, navigation, and control engineering function for the mission by autonomously imaging each asteroid target during approach and allowing the spacecraft's onboard-determined centroid of the asteroid's location in the field of view to update the IPP's knowledge of the position of the object (Good et al., 2022). Accurate knowledge of the position of the asteroids in the TTCam images will allow Lucy's higher spatial resolution instruments to achieve the best possible pointing.

However, the TTCams also have secondary uses as science cameras that can help to fulfill some of the goals of the Lucy mission (Levison et al., 2021; Bell et al., 2023). Specifically, after the terminal tracking activity is complete (just a few minutes before each closest approach), TTCam images will continue to document the spatially-resolved radiance of all of the sunlit parts of each asteroid over a wide range of phase angles. These images will help to significantly constrain the shape and thus the volume of the target asteroids (and thus, when combined with mass estimates from the mission's gravity experiment, their densities), as well as characterize their surface geology. Additional de-

Figure 1. The two TTCam camera heads on the Lockheed Martin-built Lucy spacecraft at the Astrotech testing facility in Florida, being inspected by Ryan Bronson of Collins Aerospace, the manufacturer of the TTCam optics. For scale, each camera's semi-conical sunshade is ≈15 cm long. Lockheed Martin photo PIRA #SSS2023010009, used with permission. Photo credit: Michael Ravine/Malin Space Science Systems.

tails on the science goals and measurement requirements for the TTCams is provided by Bell et al. (2023).

This paper describes the pre-flight and initial in-flight calibration of the TTCam flight instruments. Section 2 describes the pre-flight instrument characterization measurements, including linearity, scale factor, dark current, responsivity, and more. Section 3 describes the data calibration pipeline for TTCam science data. Section 4 describes the in-flight validation of our calibration measurements.

2 Pre-flight Characterization Measurements and Results

Pre-flight characterization measurements, taken both at room temperature and in a thermal-vacuum (TVAC) chamber, were analyzed for assessing the performance of the optical chain and of the 12-bit CMOS detector and electronics signal chain. Pre-flight calibration data were taken at the Malin Space Science Systems (MSSS) facility where the cameras were assembled, in San Diego, California. Calibration images were acquired with both flight cameras as well as a flight spare, and at four different sensor analog gain settings (1.0, 1.5, 2.0, and 3.5, with 1.0 being the default used for flight observations). Analysis of much of the calibration data set was carried out independently by researchers at both MSSS and ASU, with results in good agreement. Here, we present the consensus results of the analyses of the pre-flight calibration data, focusing primarily on sensor and optics performance.

2.1 Linearity

To verify the linearity of the detector, we took images of an integrating sphere fitted with a quartz-tungsten halogen (QTH) light source at different effective exposure times, from zero and up to (and beyond) exposures resulting in detector saturation. Figure 2 shows representative responses of the detectors as a function of exposure time, which we calculated with the average value of a centered 500x500 active pixel region at an analog gain setting of 1.0. Analysis of the TTCam1 detector data from between 178 12-bit Data Numbers (DN; 10 DN above the bias level) to around 4050 DN shows a maximum deviation of 1.9% from a linear fit. Analysis of the TTCam2 detector showed a similar linearity fit between 179 DN and 4007 DN, with a maximum deviation of 2.2%. More discussion on linearity, centered on calculations of the detector full well, are provided in the next section.

2.2 System Scale Factor, Read Noise, and Full Well

The same QTH light source and integrating sphere were used to collect a series of images designed so that the photon transfer method of Janesick et al. (1987) could be used to derive the sensor and electronics system scale factor g (e^-/DN) (sometimes referred to more generically as the "gain"), as a function of the sensor's analog gain state as set in the camera head electronics. Starting with an equation describing the raw signal seen on a pixel in DN, decomposed into its components:

$$S_{DN} = N_{e^-}/g + b_{DN} \tag{1}$$

where N_{e^-} is the number of electrons detected in each pixel, b_{DN} is the bias offset level in DN, and $\sigma_{R,DN}$ is the read noise of the sensor in DN. Propagation of errors gives us an equation for the variance of the raw signal in DN^2:

$$\sigma^2_{S,DN} = \frac{\sigma^2_{N,e^-}}{g^2} + \sigma^2_{R,DN} \tag{2}$$

where the read noise floor variance has been added. We can rewrite as

$$\sigma^2_{S,DN} = \frac{N_{DN}}{g} + \sigma^2_{R,DN} \tag{3}$$

since $\sigma^2_{N,e^-} = N_{e^-}$ due to photon counting (Poisson) statistics. The point of photon transfer analysis is to (1) determine the read noise, and (2) determine the system scale factor, so we rewrite the above equation as:

$$g = \frac{N_{DN}}{\sigma^2_{S,DN} + \sigma^2_{R,DN}} \tag{4}$$

Now we can consider two images of identical uniform "flat fields". The difference between these identical flat field images, $FLATDIFF$, can be defined as:

$$< FLATDIFF >=< S_{DN,1} - S_{DN,2} > \tag{5}$$

Error propagation gives us:

$$\sigma^2_{FLATDIFF} = \sigma^2_{S,DN,1} + \sigma^2_{S,DN,2} = 2\sigma^2_{S,DN} \tag{6}$$

Now consider two bias, or 0 ms exposure images. For each image, the signal in each pixel can be described as:

$$B_{DN} = b_{DN} \pm \sigma^2_{R,DN} \tag{7}$$

We can then define the $BIASDIFF$ as:

$$< BIASDIFF >=< B_{DN,1} - B_{DN,2} >=< \sigma_{R,DN,1} - \sigma_{R,DN,2} > \tag{8}$$

And in terms of σ,

$$\sigma^2_{BIASDIFF} = \sigma^2_{B,DN,1} - \sigma^2_{B,DN,2} = 2\sigma^2_{R,DN} \tag{9}$$

Going back to equation 3, we can now plug in our equations for $\sigma^2_{S,DN}$ and $\sigma^2_{R,DN}$ to get:

$$g = \frac{N_{DN}}{\sigma^2_{S,DN} + \sigma^2_{R,DN}} \tag{10}$$

$$= \frac{2N_{DN}}{\sigma^2_{FLATDIFF} + \sigma^2_{BIASDIFF}} \tag{11}$$

$$= \frac{2(S_{DN} - B_{DN})}{\sigma^2_{FLATDIFF} + \sigma^2_{BIASDIFF}} \tag{12}$$

$$= \frac{[(< S_{DN,1} > + < S_{DN,2} >) - (< B_{DN,1} > + < B_{DN,2} >)]}{\sigma^2_{FLATDIFF} + \sigma^2_{BIASDIFF}} \tag{13}$$

To use the photon transfer method, pairs of images were taken of the integrating sphere at increasing exposure times, and then the average signal level of a centered 500 by 500 pixel box was plotted against the variance of the values in that box, after subtracting the bias. Following Janesick et al. (1987), the scale factor was calculated as the inverse of the slope of the linear portion of the photon transfer curve, the read noise was calculated as the intercept of the linear fit, and the full well was determined at the "knee" point where the photon transfer curve deviates from linearity. Figure 2 shows the resulting photon transfer curves at an analog gain setting of 1.0 for each camera. Table 1 summarizes the results of the photon transfer and linearity analysis. With this gain and readout noise, the system is photon-noise-limited for signals larger than about 300 DN.

2.3 Dark Current and Bias Offset Level

The TTCam sensor electronics adds a constant offset bias voltage to every raw image that equals a 12-bit DN value of 168. In addition, CMOS sensors are known to produce a small amount of dark current (signal produced by thermal electrons), especially at elevated temperatures. In order to characterize the temperature dependence of the

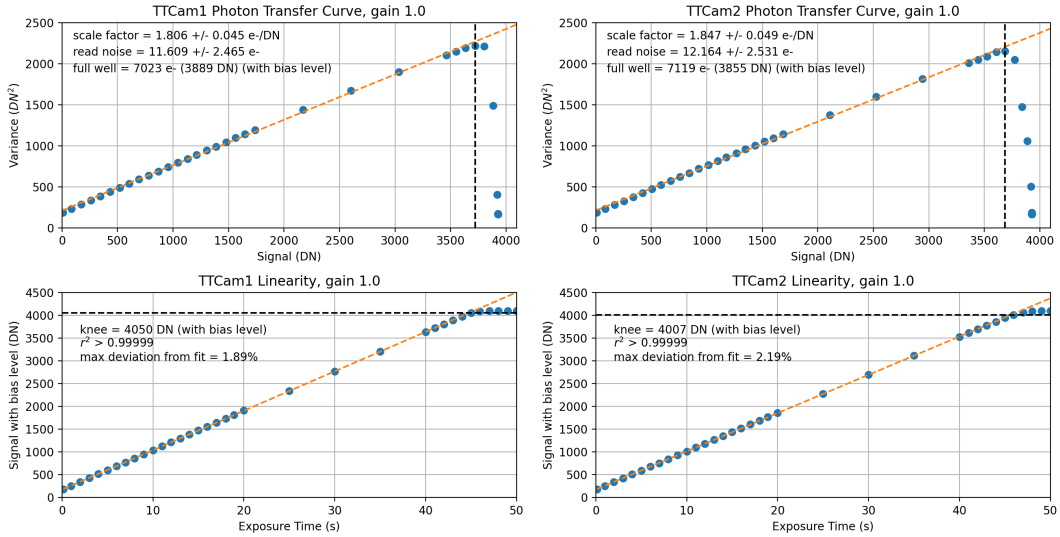

Figure 2. Photon transfer analysis and linearity of the TTCam1 and TTCam2 sensors.

Table 1. Photon Transfer Analysis Results

Camera	Scale Factor (e^-/DN)	Read Noise (e^-)	Full Well (e^-)	Deviation from Linearity
TTCam1	1.806 ± 0.045	11.609 ± 2.465	7023	1.89%
TTCam2	1.847 ± 0.049	12.164 ± 2.531	7119	2.19%

dark current as well as to search for any potential temperature dependence of the bias signal, a series of non-illuminated images at a constant exposure time (2 sec) were taken with the cameras in a thermal vacuum chamber over a wide range of potential in-flight observation temperatures. The average and standard deviation were calculated from the center half portion of the active sensor array (see Figure 6) for each camera. No temperature-dependent bias variations were observed over the expected temperature range of flight observations. Any anomalous deviations in pixel by pixel dark current behavior is noted through bad pixel flagging in the calibration pipeline, as described in section 3.2.1.

We can model the dark current, D, in DN as a response to temperature with an exponential function of the following form:

$$D = C_1 + C_2 \exp C_3 T \tag{14}$$

where C_1 is the bias offset (either 168 DN or 0 DN, depending on the companding mode as described in Section 3.1.1), C_2 and C_3 are constants, and T is the camera head temperature in °C. Figure 3 shows the resulting data and model fits for the bias and dark current model for an analog gain setting of 1.0, the setting used in flight, for each flight camera. Table 2 summarizes the parameters of the TTCam dark current model for an analog gain setting of 1.0, including an assessment of the uncertainties on the derived model coefficients. Assuming that the cameras will typically be operating below around -10°C during the Trojan flybys, no measurable dark current would be expected in TTCam images. Dark current correction will only be applied to images taken at an operating temperature above the threshold point at which the dark current is nonnegligble (>1% above background), as shown in Figure 3.

Table 2. Dark model parameters

Camera	Companding mode	C_1	C_2	C_3
TTCam1	Square root	0.000407 ± 0.000008	0.000092 ± 0.000008	0.097216 ± 0.001770
	Linear	0.015161 ± 0.000008	0.000092 ± 0.000008	0.097216 ± 0.001770
TTCam2	Square root	0.001446 ± 0.000039	0.000268 ± 0.000055	0.105134 ± 0.005696
	Linear	0.156846 ± 0.000268	0.000268 ± 0.000055	0.105134 ± 0.005696

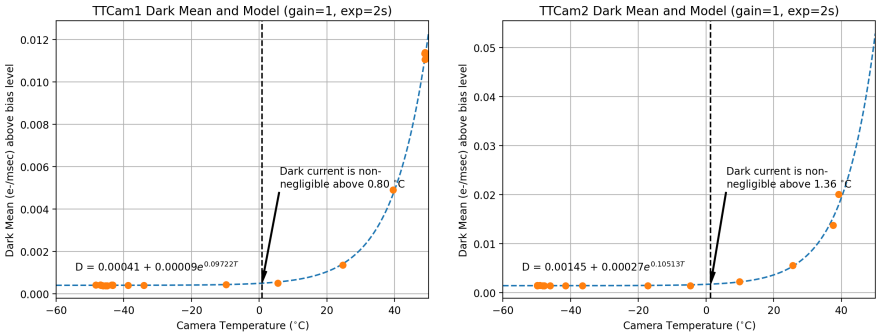

Figure 3. Dark current analysis of the TTCam1 (left) and TTCam2 (right) sensors. Each curve was fitted to an exponential model, and the point where dark current was determined to be nonnegligible was determined by finding the point on the model where the dark current rises >1% above the background level.

2.4 Pixel Responsivity Variations ("Flat Field") Characterization

Several hundred flat field images were taken with each camera by imaging into a uniform integrating sphere at a variety of camera orientations. A master flat field was created for each flight model by averaging six of the flat field images acquired at an analog gain setting of 1.0, each normalized by exposure time, and then normalizing the overall average so that its mean is 1.0. Figure 4 shows the master flat field images created for each flight model. When zooming in on small groups of pixels in these master flat field files, a faint 2x2 "checkerboard" pattern becomes apparent. This is because there are actually four independent signal chains handling the analog-to-digital conversion of each 2x2 pixel section of the sensor, in order to accommodate an optional 2x2 Bayer color pattern filter array that is not used in this monochrome application of the sensor. Despite the small differences in responsivity among these four signal chains, the standard deviations of the normalized master flat fields are ± 0.0058 and ± 0.0059 for TTCam1 and TTCam2, respectively, showing that these science-focused flat field images meet the SNR ≥ 100 requirement (Bell et al., 2023). We examined and processed additional flat field images acquired in other orientations and at other exposure times, but did not see any statistically-significant variations compared to the master flat fields described above.

2.5 Bad Pixel Maps

No "always fully unresponsive" or "always fully saturated" pixels were identified in images from either flight TTCam. To search for evidence of whether some pixels have anomalously high or anomalously low responsivity compared to the average, we looked at the ratio of two averaged flat field images at different exposure times, and compared those values to the ratio of their exposure times. We were not able to identify any such anomalously-responsive pixels that deviated more than 1% above or below the ratio of

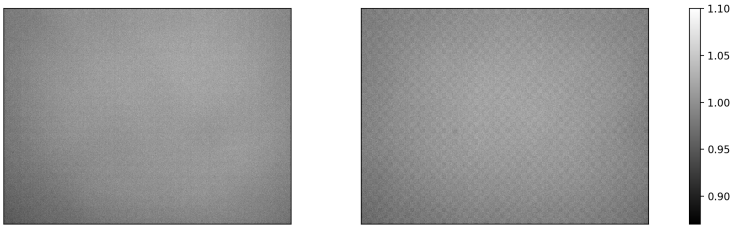

Figure 4. (left) Flat field for TTCam1. (right) Flat field for TTCam2.

Table 3. Calculated IFOV and FOV for the TTCam Flight Instruments

Camera	IFOV ($\mu rad/pix$)	Horizontal FOV	Vertical FOV	Diagonal FOV
TTCam1	73.9	10.97°	8.23°	13.71°
TTCam2	73.6	10.94°	8.20°	13.67°

the exposure times, in either flight camera. We created what we call master bad pixel maps for each camera that flag any identified "bad" pixels by assigning a value of 0 to good pixels, and 1 to bad pixels. Since we found that there were no intrinsically dead, always saturated, or anomalously-responsive pixels in either flight sensor prior to launch, the initial pre-launch master bad pixel maps are simply full active-area (see Figure 6) 2592x1944 pixel images of all 0's for both flight cameras. During the calibration of in-flight data products, however, any saturated or nonlinear pixels are also flagged in a separate unique bad pixel map that accompanies each calibrated image (see Section 3.2.1 below).

2.6 Instantaneous Field of View (IFOV), Field of View (FOV), and Geometric Distortion

The field of view of the flight TTCams was measured by mounting the instruments on a precision rotation stage and imaging a circular target at varying angular positions, at room temperature and pressure. The center of the target was calculated for each image, and the center location versus angle was used to compute the IFOV. The FOV was then calculated by multiplying the derived IFOV by the 2592 by 1944 pixel size of the active area of the sensor (Figure 6). The results for the two flight units are presented in Table 3.

Robust distortion measurements of the TTCam optics could not be made during pre-flight calibration, partially because of the long focal length of the cameras. However, the lens manufacturer (Collins Aerospace) measured the distortion of the lens assemblies at the component level before delivery to MSSS, and the worst-case distortions at the extremes of the diagonals were reported to be 0.11% for TTCam1 and 0.10% for TTCam2. These very low distortion values were qualitatively confirmed by inspection of the images used to calculate the IFOV and FOV above, and the similarly low level of distortion in flight was characterized by observations of well-known star clusters (see Section 4.5).

2.7 Modulation Transfer Function (MTF)

The system MTF of the TTCam flight cameras was estimated from images of buildings and other features observed in focus at a distance (∼hundreds of m to ∼1 km) and

photographed under ambient pressure and temperature conditions out of an open window in one of the cleanrooms at MSSS. Sharp linear bright/dark edges of features (like bright walls and dark windows, or edges of buildings against the sky) were used to estimate the contrast at the Nyquist frequency of the detector (227 lp/mm). The results indicated estimated system MTF values at Nyquist of 0.16 for TTCam1 and 0.14 for TTCam2. Even though these MTF results exceed the system level requirement (0.1), they are still considered to be only minimum estimates because the images were taken in uncharacterized conditions of atmospheric humidity or haziness and the optical system's performance was tuned for vacuum conditions. Thus, MTF is expected to be greater in flight and excellent image quality has indeed been confirmed from cruise images of stars, the Earth, and the Moon (see Section 4).

2.8 Pre-Flight Radiometric Coefficients

Pre-flight analysis of the wavelength-dependent properties of the TTCam sensors and optics (Appendix A) were used to derive estimated initial radiometric coefficients that can be used to convert values of calibrated DN/sec to physical units of radiance. Consistent with the definition of the coefficient as shown in Equation 18 below, initial values can be estimated from advance component-level knowledge of the system scale factor, the transmission and throughput of the optics, and the quantum efficiency of the sensor. Based on the component-level data for the system, an initial radiometric calibration coefficient of 0.00034 $(\frac{s}{DN})\mu W/cm^2/sr$ over a wavelength range of 420 to 680 nm was derived for both TTCam1 and TTCam2. Validation and refinement of these initial radiometric coefficients in flight for each camera is discussed in Section 4.2.

3 Data Reduction and Validation

3.1 Onboard Image Processing

3.1.1 12-bit to 8-bit companding (and decompanding)

"Companding" is a portmanteau blend of the words "compressing" and "expanding," and refers to the process of compressing the original 12-bit (0-4095) DN values of each raw TTCam pixel onboard down to 8 bits (0-255) of dynamic range, and then expanding the data back to 12-bit in ground data processing after downlink. Companding is nominally performed in what is called "mode 17" (0x11 in hex) using an onboard square-root-based lookup table (Appendix B) to scale the data down to a smaller number of bits per pixel so that Poisson (shot) noise is not encoded or downlinked in the telemetry (e.g., Malin et al., 2013; Bell et al., 2017). The opposite process, expanding the downlinked 8-bit pixel values back to an estimate of their original linear 12-bit values, is referred to as "decompanding," and is part of the initial process that the Lucy Science Operations Center (SOC) uses to create the raw TTCam Uncalibrated Data Products (UDPs) for use by the science team. The default lookup table to convert 8-bit square-root companded mode 17 downlinked images back to 12-bit values is presented in Appendix C. While the onboard 12-bit to 8-bit square-root companding lookup table can be modified in flight if needed, the expectation is that the mode 17 TTCam lookup table in Appendix B will nominally be the default for tracking and encounter mode images acquired during the entire mission. During cruise, other linear companding modes such as divide-by-16 (mode 27; 0x1b), or least-significant-bits only (mode 19; 0x13) are also being tested, as ways to validate the radiometric calibration of the images when using the nominal default square-root mode. The subtraction of the bias level of 168 DN is dependent on the companding mode. Square root companding will return pixel values with the bias level pre-subtracted. Otherwise, the bias subtraction will still be performed in the calibration pipeline (see section 3.2.2). Regardless of the companding mode used, all TTCam flight images will nominally be downlinked to Earth as 8-bit companded images.

3.1.2 Lossless (PPMd) Compression

TTCam images are transferred from the camera head to the DVR and stored in flash memory as uncompressed raw images. Compression of the raw images is achieved in two steps: first, the images are compressed from 12-bit to 8-bit using a square-root-like lookup table as described above (the default for tracking and encounter imaging) that avoids encoding of shot noise in the output 8-bit data. Then the 8-bit images are transferred to the spacecraft computer where they are subsequently compressed further using the PPMd compression algorithm. Additional details on TTCam onboard image compression are provided by Bell et al. (2023). As a benchmark, using this combination of companding and lossless compression, compression ratios of 3:1 to 4.5:1 have been achieved in the downlinked data volume for early cruise star field images.

3.2 Radiometric Calibration Pipeline

To help create the highest possible quality TTCam data set for science and archival purposes, we developed a radiometric calibration pipeline which takes as input the decompanded 12-bit raw images, camera ID, temperature, exposure time, the radiance of the Sun in the TTCam bandpass at the heliocentric distance of the observation, and a set of pre-flight and in-flight derived ancillary calibration files to convert raw data to units of radiance and radiance factor (or I/F, defined below). The pipeline corrects for bad pixels, dark current, bias offset, and pixel-to-pixel responsivity (flat field) variations, and scales the pixel data values by the derived radiometric calibration coefficient. Figure 5 provides a flow chart of the calibration pipeline.

We can also summarize the calibration pipeline mathematically, starting with an equation describing the components of the raw signal $DN_{i,j}$ that are measured by a single pixel (i, j):

$$DN_{i,j} = \frac{A_o \Omega t_{exp}}{g F_{i,j}} r_0 \int_\lambda r_\lambda L_\lambda \frac{\lambda}{hc} d\lambda + B_{i,j} + D_{i,j} \tag{15}$$

where $A_o\Omega$ in [m^{2}sr] is the entendue, or optical throughput; t_{exp} in [sec] is the exposure time; g in [e$^-$/DN] is the system scale factor, $F_{i,j}$ [unitless] is the normalized relative responsivity of that pixel (flat field); $B_{i,j}$ in [DN] is the bias offset; $D_{i,j}$ in [DN] is the dark current; r_0 in [e$^-$/ph] is the weighted quantum efficiency; r_λ [unitless] is the weighted optical transmission; L_λ in $[\frac{W}{m^2 srnm}]$ is the spectral radiance incident on the aperture; and $\frac{\lambda}{hc}$ in [ph/J] is the conversion factor between energy and photon flux.

Via calibration, we want to ultimately derive the mean, bandpass-integrated spectral radiance incident on the camera's front aperture. We can define this value as:

$$< L_\lambda >= \frac{\int_\lambda r_\lambda L_\lambda \frac{\lambda}{hc} d\lambda}{\int_\lambda r_\lambda \frac{\lambda}{hc} d\lambda} \tag{16}$$

Plugging in equation 15 for the numerator in equation 16 gives us:

$$< L_\lambda >= \frac{g F_{i,j}}{A_o \Omega t_{exp}} \frac{DN_{i,j} - B_{i,j} - D_{i,j}}{r_0 \int_\lambda r_\lambda \frac{\lambda}{hc} d\lambda} \tag{17}$$

We can then define a radiometric calibration coefficient r such that

$$r = \frac{g}{A_o \Omega r_0 \int_\lambda r_\lambda \frac{\lambda}{hc} d\lambda} \tag{18}$$

where r_0 is the weighted quantum efficiency and r_λ is the weighted optical transmission. This allows us to simplify equation 17 to:

$$< L_\lambda >= \frac{r F_{i,j}}{t_{exp}} (DN_{i,j} - B_{i,j} - D_{i,j}) \tag{19}$$

Equation 19 forms the basis of the TTCam calibration pipeline.

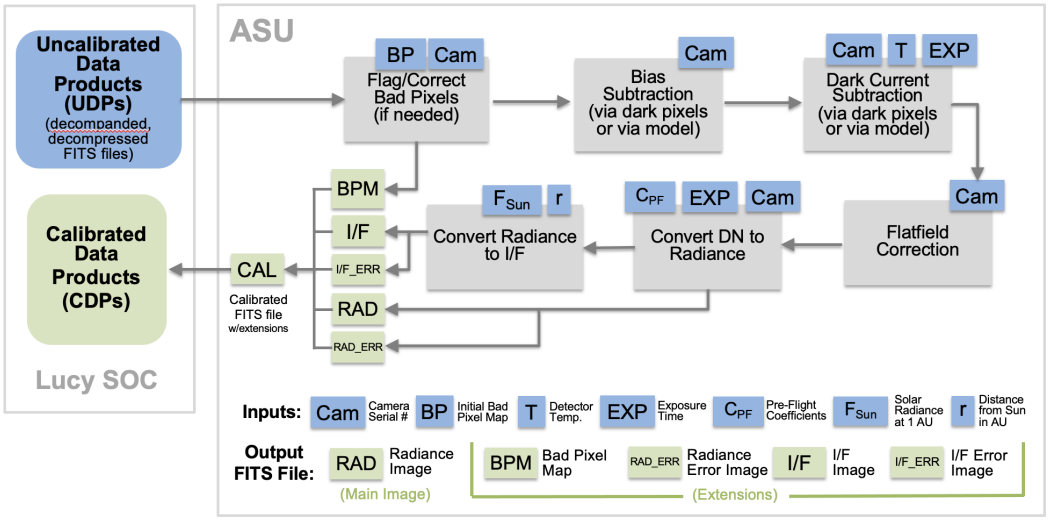

Figure 5. Flowchart of the TTCam calibration pipeline.

Table 4. Flagged nonlinearity and saturated pixel values

Camera	Companding mode[a]	Non-linearity flag	Saturated flag
TTCam1	Square root	3721	3923
TTCam1	Linear	3889	4080
TTCam2	Square root	3687	3923
TTCam2	Linear	3855	4080

[a]See Section 3.1.1

3.2.1 Bad Pixel Flagging

Before any calibration and conversion of the data, we first flag any bad pixels. The pipeline defines four different categories of bad pixels: (1) Saturated pixels, (2) Nonlinear pixels, (3) Bad pixels (dead or hot pixels) as flagged in the master bad pixel map (Section 2.5), and (4) pixels with original 12-bit values below the constant 12-bit bias offset level of 168 DN.

For the bad pixel map, the calibration pipeline outputs a FITS extension of the same size as the uncalibrated image, with a value of 0 for each pixel, and checks each raw image for any always-saturated or always-zero pixels (flagging them with a value of 1; see Section 2.5), or saturated or nonlinear pixels based on scene brightness and companding mode (see Table 4), flagging them with a value of 2 for any saturated pixels, and a value of 3 for any nonlinear pixels (not inclusive of saturated pixels). Then the pipeline corrects for bad pixels in the bad pixel map input by replacing each bad pixel with the median of its eight immediately-surrounding pixels.

3.2.2 Bias Subtraction

For images acquired using linear 12-bit to 8-bit companding methods (modes 19 or 27; see Section 3.1.1), bias removal is included as part of the dark current subtraction process (next section), because it involves a simple subtraction of the constant bias level of 168 in 12-bit DN space. However, for images acquired using square-root companding (mode 17), the 168 DN bias is automatically subtracted prior to downlink within

the camera electronics, in 12-bit DN space and prior to companding the images to 8-bit space. In the latter case, expected to be the vast majority of downlinked TTCam images, bias subtraction is not performed by the calibration pipeline.

3.2.3 Dark Current Subtraction

The bias and dark current correction is dependent on a number of factors. First, the pipeline checks if the camera head temperature at the time of the observation from the raw data file's "T2CCHTMP" FITS header value exceeds a certain value, which our dark current analysis has determined to be the threshold value over which dark current is nonnegligible (see Section 2.3). If image temperature is under that threshold value, which will most likely always be the case during flight, then only bias subtraction needs to be performed. Bias subtraction is dependent on the companding mode of the image (see Section 3.2.2).

If the camera head temperature is recorded to be higher than the threshold value, then the dark current contribution to the image is nonnegligible, and dark current correction is needed. This dark current subtraction can happen in one of two ways. First, the pipeline checks if the raw data file contains the standard masked dark pixel region (as defined in Figure 6), and if it does, it will use the average and standard deviation of the pixels in that region (specifically, the average and standard deviation of the zero-based pixels in rows 1970 to 1993 and columns 16 to 2607; see also Bell et al., 2023) to perform the correction. This is the standard and most robust method of subtracting the bias and dark current background signal from the raw data acquired for TTCam calibration. However, if the standard masked dark pixels have not been downlinked (as will be the case for the smaller 2592x1944 pixel active-area-only terminal tracking and science images acquired during each asteroid encounter), the pipeline instead uses the dark current model and parameters described in Section 2.3 and in Table 2 and the camera head temperature at the time of the observation to calculate the dark current value to subtract.

3.2.4 Pixel-to-Pixel Responsivity Variations ("Flat Field") Correction

The normalized flat field array for each camera from Section 2.4 above is divided out of the bias- and dark current-subtracted image at this step.

3.2.5 Radiometric Conversion

Referring back to equation 19, the radiometric coefficient r converts our reduced data to calibrated physical units. Error propagation on equation 19 gives us the following error calculation:

$$\sigma^2_{<L_\lambda>} = \left(\frac{<L_\lambda>\sigma_r}{r}\right)^2 + \left(\frac{<L_\lambda>\sigma_{F_{i,j}}}{F_{i,j}}\right)^2 + \left(\frac{rF_{i,j}}{t_{exp}}\sigma_{DN_{i,j}}\right)^2 + \left(\frac{rF_{i,j}}{t_{exp}}\sigma_D\right)^2 \quad (20)$$

where $\sigma_{DN_{i,j}}$ is calculated from Poisson distribution statistics on the number of electrons generated by each pixel detector, and $\sigma_{F_{i,j}}$ and σ_D are the standard deviations of the averaged flat fields and dark current values, respectively.

The output of the radiometric conversion is a calibrated image the same size as the uncalibrated image, represented in physical radiance units ($\frac{\mu W}{cm^2 sr}$) instead of DN, and an associated extension image of the same size with the radiance error on each pixel in the same radiometric units as the calibrated image.

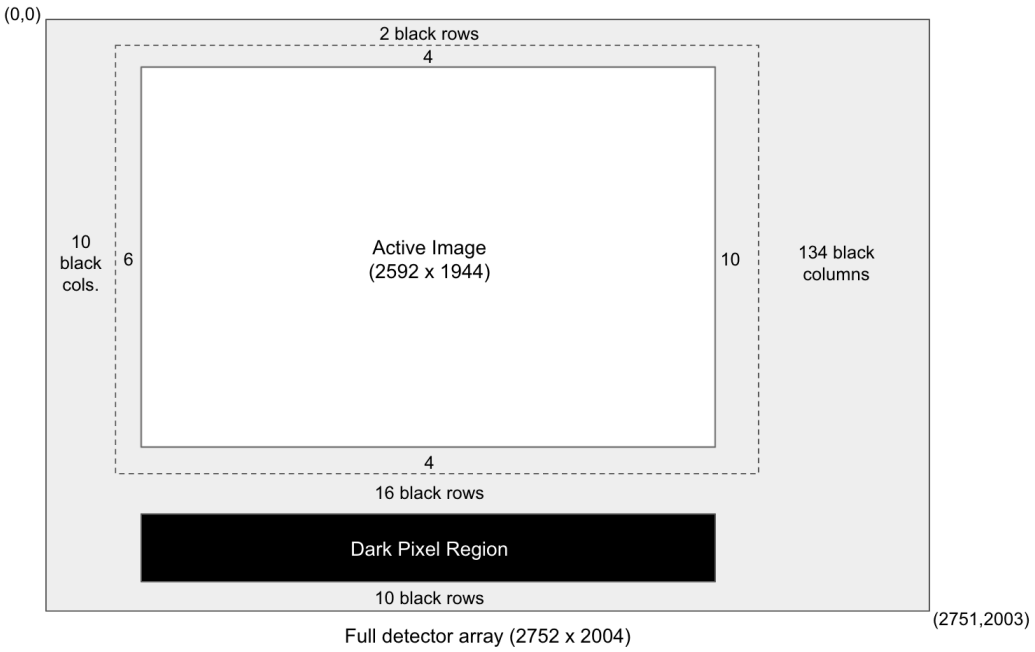

Figure 6. Cartoon diagram of the full TTCam CMOS detector array, showing the active image area and the masked pixel region (area sizes are not shown to scale). Pixels in the black region (zero-based rows 1970:1993 and columns 16:2607) are used for the assessment of bias and dark current signals for calibration images where these sensor pixels are downlinked. Because of a limit on the image size that can be transferred into the spacecraft's terminal tracking algorithm, however, only the pixels in the 2592x1944 active area are read out during each asteroid encounter. When typical 2592x2000 pixel calibration images are read out, the gray areas are ignored in processing.

3.2.6 I/F Conversion

It is often convenient to convert calibrated images of spatially resolved solar system objects that reflect sunlight from radiance to radiance factor, also known as "I/F", where I is the incident radiance measured from the object of interest (calculated in Section 3.2.5 above), and πF is the irradiance of sunlight incident on the object at the time of the observation (e.g., Hapke, 2012). I/F is sometimes referred to as "approximate reflectance" because such values can be directly compared to a variety of laboratory absolute reflectance measurements of analog rock, mineral, and/or ice samples. In addition, I/F divided by the cosine of the solar incidence angle of the surface being imaged is an excellent approximation for the Lambertian albedo of a surface, if indeed that surface acts like an isotropic scatterer.

Starting with radiance calibrated data as described above, I/F for calibrated TTCam images is calculated using the following formula:

$$I/F = \frac{< L_\lambda >}{f_{sun}/H_d^2/\pi} \tag{21}$$

where $< L_\lambda >$ is the mean, bandpass-integrated radiance, f_{sun} is the solar radiance convolved over the TTCam bandpass at 1 AU (assumed to be 57546.591 $\frac{\mu W}{cm^2 sr \mu m}$ for both flight cameras), and H_d is the heliocentric distance of the target body at the time of the observation, in AU. I/F is dimensionless, and I/F images of objects that are not reflecting sunlight (e.g., stars) will not have any particular physical meaning. Derived unitless I/F values for each pixel are stored in an additional associated extension image of the same size as the calibrated image.

The I/F error is calculated by propagating the radiance error through the I/F calculation. The following formula gives I/F error:

$$\sigma_{I/F} = \frac{\sigma_{<L_\lambda>}}{f_{sun}/H_d^2/\pi} \tag{22}$$

Derived unitless I/F error values for each pixel are stored in an additional associated extension image of the same size as the calibrated image.

4 In-Flight Calibration and Validation

During the cruise portion of the Lucy mission, a series of instrument checkouts and flight tests are being performed to validate the performance of the instruments. Figures 7 and 9 below show sample cruise images from some of these instrument checkout activities. Below, we discuss how these activities to date are pertinent for the calibration and validation of the TTCam instrument.

4.1 Dark Current Model Validation

The first few in-flight calibration activities revealed the extent of how alternate companding modes affected the bias level and consequently our calculations of the dark current contribution.

The first instrument checkout revealed a higher than expected average from the dark pixel region due to the clipping of negative-value pixels after automatic subtraction of the 168 DN bias level during square root companding. Apparently, many of these sky pixels must have had original 12-bit DN values less than the 168 DN bias level. Figure 8 shows this effect graphically, and also reveals how the presence of the bias level, which is dependent on the companding mode, affects the average of the dark pixel region, and consequently affects our method of calculating the expected dark current level, as explained in Section 3.2.3. Regardless, in TTCam images acquired during the first few years

Figure 7. The Rosette Nebula (just to the right and below center) and associated star field in the constellation Monoceros centered near 06h 29m 38.568s RA, +07° 03' 00.642" Dec. Image acquired by TTCam1 on 14 Feb. 2022 during the Launch+120 TTCam cruise imaging campaign.

of cruise at temperatures between -10°C to -30°C, we have seen no detectable evidence of dark current signal in the raw data with exposure times up to 30s. This is consistent with the dark current model from pre-flight analysis, which predicts no statistically significant dark current below ≈0°C.

4.2 Extended Object Radiometry

One of the primary objectives of the TTCam calibration is to calibrate images for science objectives, which requires an accurate understanding of the radiometric conversion from instrument-specific units to universal physical radiance units. Pre-flight analysis of the instrument's optical throughput, scale factor, quantum efficiency, etc. gave us an analytical estimate of the radiometric conversion factor, which we called the radiometric coefficient. However, observations of the Earth and Moon during the gravity assists that are a part of Lucy's orbital tour give us the opportunity to validate our radiometric calibration using the Moon (and, to a lesser extent, the Earth), as a "known" radiometric source. The following sections describe the in-flight validation of our radiometric calibration pipeline.

4.2.1 Radiometric coefficient validation

During Lucy's first Earth Gravity Assist (EGA1) (Spencer et al., 2024) on October 13-16, 2022, TTCam1 and TTCam2 data collection included 5 images of the Earth from each camera, 5 each of the Moon, and 5 each of both in the same frame. Figure 9 shows representative examples of some the various Earth and Moon images taken during EGA1. The Moon images were used for primary validation of the radiometric coefficient derived in Section 2.8, and the Earth images provided a second set of less quantitative validation observations.

In order to enable the use of the Moon as a calibration and performance-verification target, we computed a model of the Lunar reflectance (I/F) expected under the illumi-

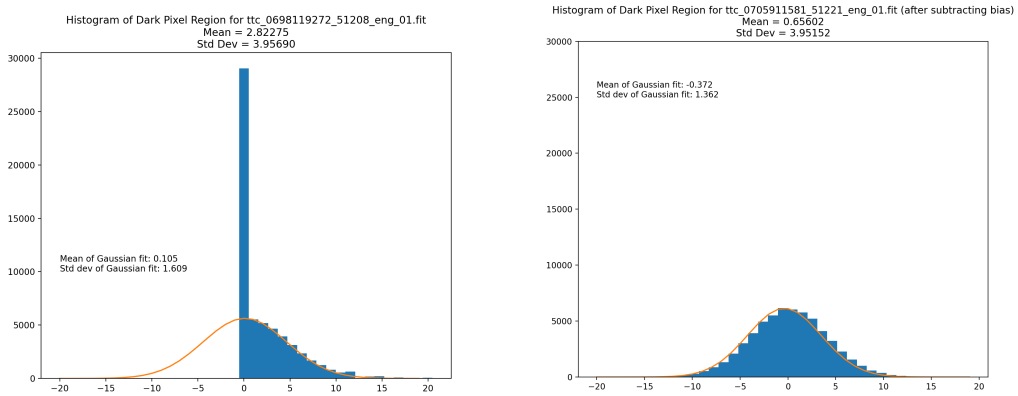

Figure 8. (left) Histogram of the dark pixel region from the Launch+20 day flight images. The absence of the bias offset created a higher averaged dark pixel region, which meant an inaccurate estimate of dark current from the dark pixel region. (right) Histogram of the dark pixel region from thee Launch+7 month flight images, where what would have been "negative DN" values in the left plot were retrieved because the bias offset is not subtracted when using the linear companding modes. The average of this dark pixel region shows minimal dark current contribution, as expected.

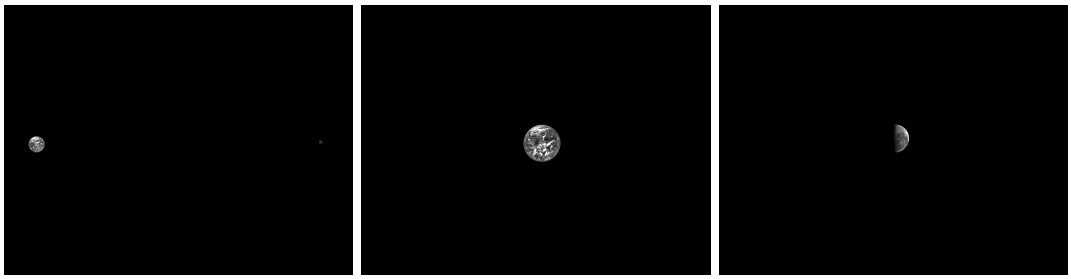

Figure 9. Example TTCam1 images from the first Lucy mission Earth-gravity assist. (left) The Earth and (much dimmer) Moon in the same field of view; 13 Oct. 2022, 11:08 UTC. Range to Earth: ∼1,440,000 km; range to Moon: ∼1,750,000 km. (middle) Best resolution TTCam1 image of the Earth; 15 Oct. 2022, 04:52 UTC. Range to Earth: ∼622,000 km. (right) Best resolution TTCam1 image of the Moon; 16 Oct. 2022, 18:14 UTC. Range to Moon: ∼246,000 km.

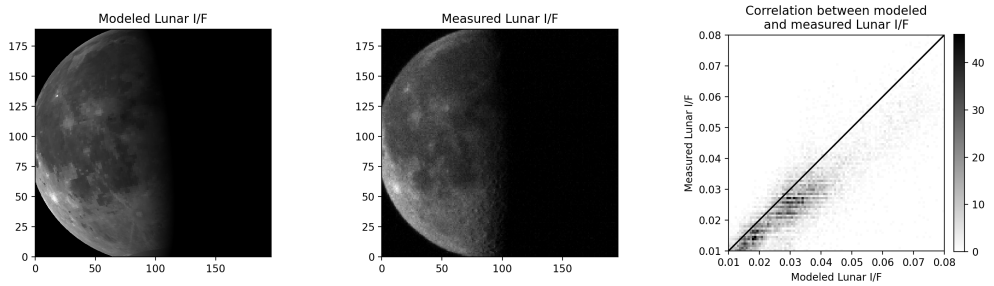

Figure 10. (left) Synthetic image of the Moon for the epoch 2022-10-16T14:45:00 UTC as seen from TTCam. (middle) The observed in-flight TTCam image of the Moon, from the file ttc_0719216033_51253_eng_01_cal.fit. (right) Correlation between modeled and measured I/F values of the Moon, as a histogram of the overlapping values.

nation and viewing geometry conditions occurring during the time of EGA1. For this purpose, we used the spatially-resolved Hapke photometric parameter maps (Hapke, 2012) derived from multispectral observations by the Lunar Reconnaissance Orbiter Camera (LROC) (Sato et al., 2014). This photometric model covers the range ±70° in selenographic latitude, which corresponds to ∼94% of the whole Lunar surface, or ∼98% of the projected surface imaged by TTCam. The resolution of the model is 1° x 1° in latitude and longitude, which is comparable to the range of pixel footprint sizes on the Moon in TTCam images obtained during the encounter. We used the model parameters at 604 nm, which is close to the ∼535 nm effective center of the T2Cam transmission band (Bell et al., 2023), to generate synthetic images of the Moon at the time of the encounter. Given the comparatively low spatial resolution of the model, the Moon was represented as a perfect sphere with a radius of 1737.4 km, thereby ignoring surface topography. For this reason, the model does not capture any shadows due to topography, but only photometric variations. The relevant photometric angles were computed for the times of exposure by using the NAIF SPICE environment (Acton, 1996).

Figure 10 shows the correlation of the modeled lunar I/F values with the I/F values from the EGA1 data, as calibrated by the radiometric pipeline. The histogram shows a good correlation, indicating an agreement between the expected and actual values with a Pearson correlation coefficient of r=0.95, providing a reasonable validation of the results of our radiometric pipeline.

4.2.2 Exposure Time Modeling

Given the predicted reflectance and photometric properties of a target, we want to be able to estimate the DN and SNR of that target when imaged with TTCam. To do this, we created an exposure time model:

$$t_{exp} = (DN_{i,j} - B_{i,j} - D_{i,j}) \frac{rF_{i,j}}{< L_\lambda >} \tag{23}$$

where r is the pre-flight radiometric calibration coefficient (0.00034 $(\frac{s}{DN})\mu W/cm^2/sr$) and the other variables are as defined above. The EGA1 images gave us the opportunity to validate this exposure time model. Figure 11, for example, shows the modeled and actual signal levels from EGA1 images of the Moon. For good signal levels below nonlinearity and saturation the exposure time model appears to slightly over-predict the actual raw DN levels of the target, making the model, perhaps appropriately, somewhat conservative against saturation.

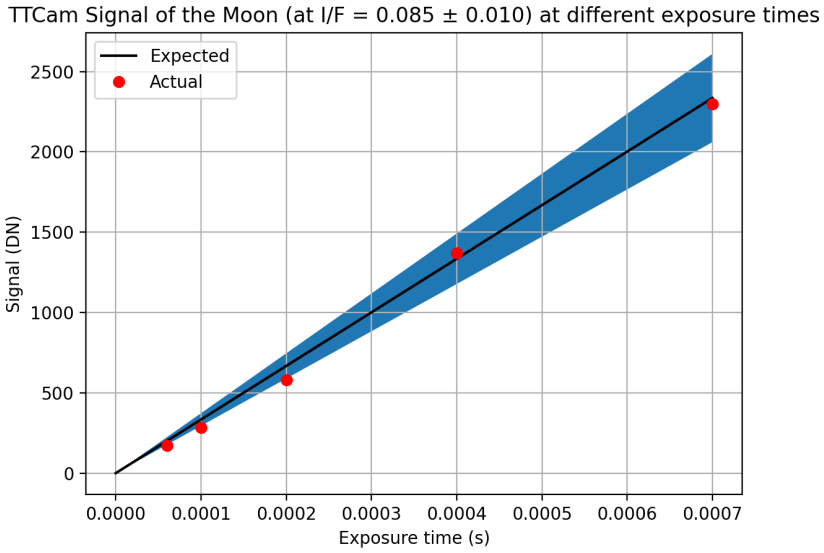

Figure 11. Exposure time model results (solid line) for a source at 1 AU with I/F = 0.1, plotted against the actual raw DN levels (data points) from EGA1 images of a region of the Moon with a model-predicted I/F = 0.085±0.010. The shaded blue region shows the range of expected signal values due the error in predicted I/F.

4.3 Point Source Observations: Linearity and Radiometric Stability

Analysis, including aperture photometry, of a variety of stellar fields observed during cruise so far (e.g., Figure 7) confirm that the extended source linearity behavior described earlier in Section 2.1 is also valid for point sources. Analysis of a series of these kinds of star observations during cruise so far also demonstrates good radiometric stability over time.

4.4 Scattered Light Testing

On March 28, 2023, when the spacecraft was approximately 1.7 AU from the Sun, a series of Lucy payload observations was acquired while pointing the fields of view of the IPP instruments sunward, to simulate the viewing geometries of future eventual asteroid encounter observations (Olkin et al., 2021) and to search for potential scattered sunlight effects at the most challenging expected Solar Elongation Angles (SEAs; SEA=0 would mean the Sun directly down the boresight). TTCam images were acquired at four different SEAs: 81° (simulating the viewing geometry on departure from the eventual Eurybates and Polymele flybys), 76° (Leucus approach), 66° (Dinkinesh approach), and 54° (Patroclus departure; the most stressing case for scattered light). Images at each SEA were acquired at both the short exposure times expected to be used during the flybys (30 msec and less), as well as at the longest-possible TTCam exposure time of 30 sec. Analysis of the images reveals no significant ghosts and only a faint linear brightness pattern on one edge of the TTCam field of view that appears to result from scattered sunlight reflecting off the lip of the aperture opening in the TTCam sunshade (see Figure 1 above, and Figure 3 in Bell et al., 2023). The peak signal level of that faint pattern in the most stressing case of SEA=54° is more than a factor of 10^5 less than the level of incident sunlight. The scattered light signal is even lower as the Sun moves even farther off the boresight at larger SEAs. As a result, scattered sunlight is expected to be

much less than 1 DN at typical exposure times of a few to a few tens of msec, meaning that it will not be a significant source of background signal or noise in eventual TTCam tracking or encounter images of any of the target asteroids. A second set of similar scattered light assessment observations will be acquired later in cruise, in colder thermal conditions once the spacecraft reaches 4 AU.

4.5 Geometric Distortion

In order to use the TTCams for optical navigation, their focal length and geometric distortion must be characterized and calibrated. We used all available long-exposure images from the Launch+20 day and Launch+120 day calibration campaign observations. Due to a lack of images at varying temperatures, we were unable to estimate a temperature dependence of the TTCam focal lengths. We aim to characterize this temperature dependency as more images at colder temperatures become available as Lucy travels into the outer solar system. In lieu of the UCAC4 star catalog described in Bos et al. (2020), the TTCam focal length and geometric distortion calibrations utilized the Gaia star catalog, which contains significantly more stars and is intrinsically more accurate.

We used the OpenCV distortion model to represent the distortion across the field (OpenCV, 2014). More information on how the OpenCV distortion model was used to estimate the focal length and geometric distortion can be found in sections 7.2 and 7.5 of Bos et al. (2020). The analytical formulation for the OpenCV model is constructed using the following equations.

A vector in inertial space, v_I, is first transformed into the frame of the image using the rotation matrix C^I_{image} such that

$$v_{image} = [C^I_{image}]^T v_I \tag{24}$$

where v_{image} is the resulting vector in the image frame with origin at the OpNav defined intersection of the boresight and of the imager. This boresight location serves as the origin of the image frame axes within the OpNav process.

The resulting vector is then projected into the image plane using the equation

$$\begin{bmatrix} x_0 \\ y_0 \end{bmatrix} = \frac{1}{|v_{image,z}|} \begin{bmatrix} v_{image,x} \\ v_{image,y} \end{bmatrix}$$

where x_0 and y_0 are the resulting image plane coordinates in the x- and y-dimensions, relative to an origin at the boresight intersection.

The geometric optical distortion is then applied using the equations

$$r^2 = x_0^2 + y_0^2$$

$$\begin{bmatrix} x \\ y \end{bmatrix} = \begin{bmatrix} x_0 & 2x_0y_0 & r^2+2x_0^2 \\ y_0 & r^2+2y_0^2 & 2x_0y_0 \end{bmatrix} \begin{bmatrix} \frac{1+k_1r^2+k_2r^4+k_3r^6}{1+k_4r^2+k_5r^2+k_6r^2} \\ p_1 \\ p_2 \end{bmatrix}$$

where x and y are the distorted image plane coordinates. The $k_{1...6}$ coefficients correspond to the radial distortion of the optical system, and the $p_{1,2}$ coefficients correspond to the tangential distortion.

The final distorted sample and line coordinates are then calculated using the equation

$$\begin{bmatrix} u \\ v \end{bmatrix} = \begin{bmatrix} f_x(1 + a_1 T)x \\ f_y(1 + a_1 T)y \end{bmatrix} + \begin{bmatrix} c_x \\ c_y \end{bmatrix}$$

where T is the camera temperature in degrees Celsius, and u and v are the distorted sample and line coordinates in units of pixels. The values f_x and f_y refer to the focal lengths of the imager along the x- and y-dimensions in units of pixels at a camera temperature of 0°C. The value a_1 is a parameter to model the temperature dependence of the focal lengths. The $k_{1,2,3}$, $p_{1,2}$, f_x, and f_y values are estimated parameters in the calibration solution. The values c_x and c_y refer to the sample and line coordinates of the OpNav defined boresight of the system in units of pixels and in the OpNav coordinate system. We do not estimate the true optical axis for TTCam, so the fixed boresight definition is used for any and all values reported. The necessary data to estimate a_1 has not been collected yet and the solved for parameters reflect the thermal conditions of the L+120 imaging activities. The remaining k_i terms are not estimated; heritage from past missions has shown that the set of coefficients used is sufficient for a precise distortion model of the instrument.

4.5.1 Geometric Distortion Calibration Results

A geometric distortion model using the OpenCV distortion model (OpenCV, 2014) was generated using a total of 2978 imaged stars for TTCam1 and 4323 imaged stars for TTCam2. The camera parameters and distortion coefficients are provided below in Table 5. Maps of the distortion solution on the FOVs are shown in Figure 12, which also shows pre- and post-fit star-center residuals in order to visualize the extent to which each model matches the optical data. Residuals are shown vs. magnitude, as well as vs. pix/line position, and as scatter-quiver plots on the FOV.

The initial pre-fit quiver plot suggests the camera modeling errors are dominated by the focal length error and radial errors near the corners, but the post-fit residuals in Figure 12 show only a hint of remaining structure near the corners.

As expected, while the pre-distortion-fit residuals have non-zero means on the order of a tenth of a pixel, the standard deviation of those residuals is quite large, on the order of a few pixels for TTCam1 and about one-half of one pixel for TTCam2. After the distortion model converged, the post-fit residuals displayed near zero means and a standard deviation of under a tenth of a pixel for TTCam1 and one-tenth of a pixel for TTCam2. Though this is not the final calibration activity or model, these statistics suggest that the current camera model is already robust.

4.5.2 Geometric Distortion Comparison

A close examination of the various pre-fit plots of the TTCams will show differences in the various characteristics of the imagers prior to the distortion calibration solution being applied.

Notably, a comparison of top-middle pre-distortion-fit plots in Figure 12 shows that the pre-fit behavior of the imagers differ greatly. While both instruments show similar pre-fit residual means, the standard deviation of those residuals is almost an order of magnitude higher for TTCam1 compared to TTCam2. Additionally, TTCam2 shows some of the correlation between residual and magnitude that we generally see in calibrated star residuals, while TTCam1 shows no such correlation and is dominated by the larger residuals. This is due to the larger focal length error in the TTCam1 a priori compared to TTCam2.

The two instruments show similar post-fit characterization, with very little structure evident in the residuals.

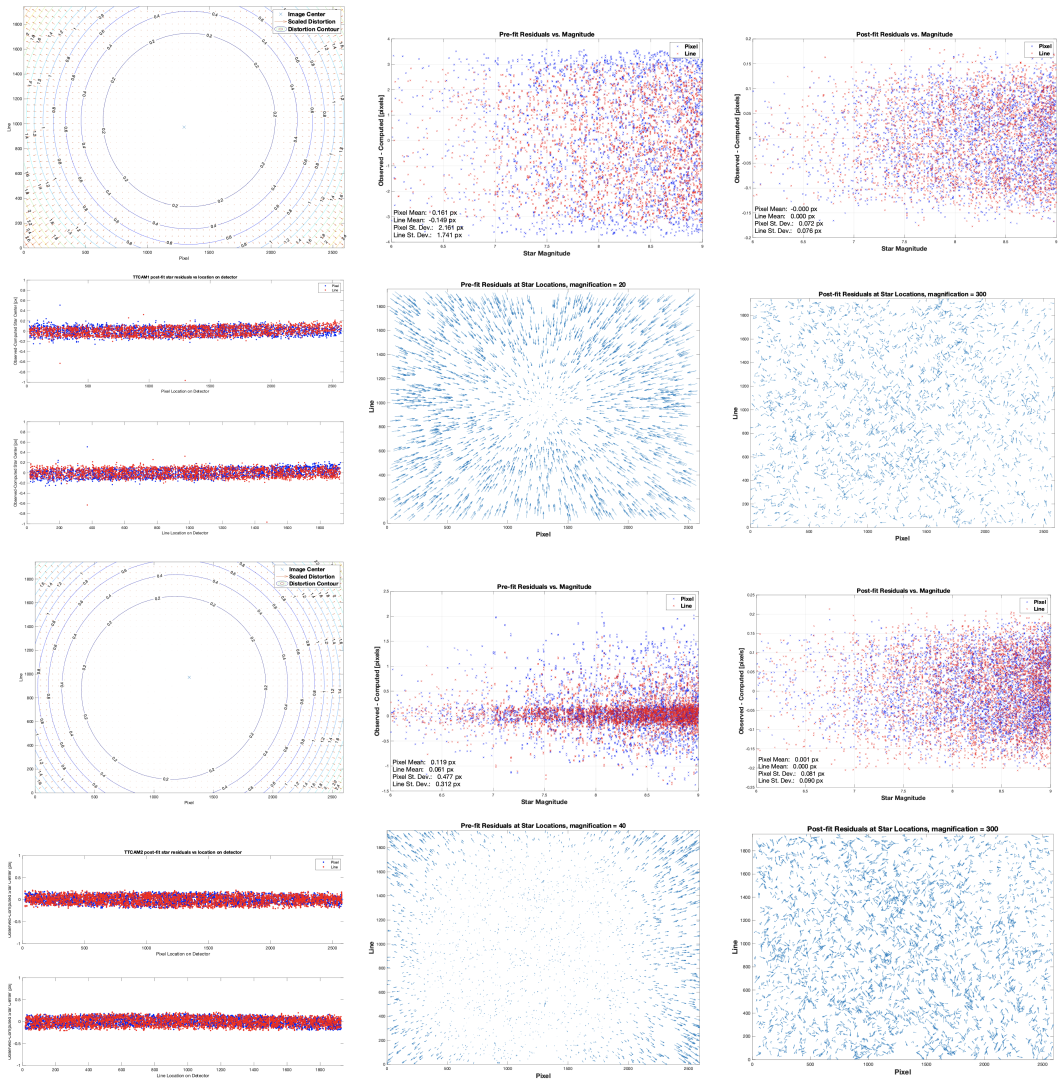

Figure 12. The top six figures refer to TTCam1, while the bottomw six figures refer to TTCam2. (top left) Post-calibration Optical Distortion Map. The contours show lines of constant distortion magnitude, and the quivers show direction and scaled magnitude of the distortion. (top middle) Pre-distortion-fit scatter plot of star center residuals vs. star magnitude. (top right) Post- distortion-fit scatter plot of star center residuals vs. star magnitude. (bottom left) Scatter plots of star center residuals using the OpenCV distortion model. The top plot presents the residuals along the Pixel (horizontal) dimension of the FOV, and the bottom plot presents the residuals along the Line (vertical) dimension. (bottom middle) Pre-distortion-fit Quiver plot of star center residuals using the OpenCV distortion model. The vector lengths have been multiplied 20x the actual residual value. (bottom right) Post-distortion-fit Quiver plot of star center residuals using the OpenCV distortion model. The vector lengths have been multiplied 300x the actual residual value.

Table 5. Estimated camera parameters and distortion coefficients for TTCam1 and TTCam2 using the OpenCV distortion model.

Camera Parameter	Value	Coefficient	Value
	TTCam1		
f_x (pixels)	13448.168	$k1$	1.074e-01
f_y (pixels)	13447.850	$k2$	3.641e-01
c_x	1296.5	$k3$	5.287e-02
c_y	972.5	$p1$	-4.641e-04
$a1$	0	$p2$	-3.310e-04
	TTCam2		
f_x (pixels)	13498.412	$k1$	7.760e-02
f_y (pixels)	13497.884	$k2$	2.275
c_x	1296.5	$k3$	2.566e-02
c_y	972.5	$p1$	5.841e-04
$a1$	0	$p2$	8.625e-04

4.6 Point Spread Function

The TTCam point spread function was assessed using standard shift and add analysis of cruise star observations, as well as modeled assuming a Gaussian profile.

4.6.1 Shift and Add Stellar PSF Analysis

The TTCam Point Spread Functions (PSFs) were estimated using the "effective Point Spread Function" (ePSF) method developed by Anderson (2016) and Anderson and King (2000) and implemented in Astropy's Photutils Python package (Bradley et al., 2023). Provided a FITS image of a star field, the process begins with a null ePSF, identifies stars above a desired threshold, and iterates between the current star being evaluated and the developing ePSF. The process involves oversampling the PSF by 4x, differencing between the current star and the developing ePSF, averaging and adjusting pixel residuals, smoothing, and re-centering over a user-provided N iterations with a final rescaling to 1x sampling. Visual inspection of stars identified is performed to remove hot pixels or stars that are too close to each other from consideration. For TTCam1, 271 stars were identified and used to estimate the final PSF using this technique, and for TTCam2, 69 stars were used.

Figures 13 provides a graphical representation of the derived PSFs for TTCam1 and TTCam2, respectively, and Table 6 provides the normalized (sum = 1.0) 7x7 pixel representations of those PSFs.

4.6.2 Gaussian PSF Modeling

The TTCam point spread function (PSF) was also modeled using the following generalized (rotated) 2D Gaussian function:

$$f(x,y) = Ae^{-[(x-x_0)(y-y_0)]BSB^T\begin{bmatrix}(x-x_0)\\(y-y_0)\end{bmatrix}} \tag{25}$$

where

$$B = \begin{bmatrix} cos(\theta) & -sin(\theta) \\ sin(\theta) & cos(\theta) \end{bmatrix}$$

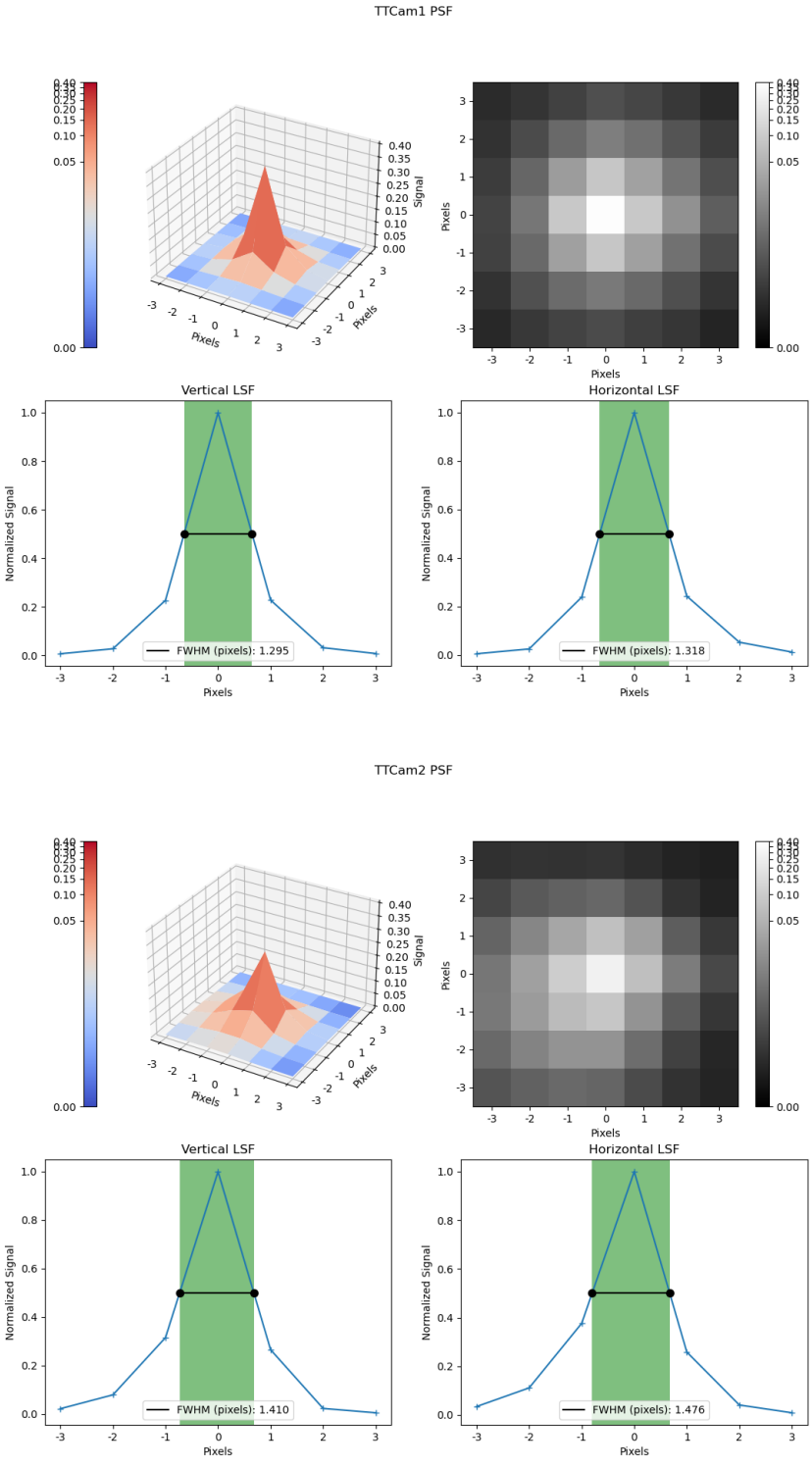

Figure 13. (top four) Estimated PSF for TTCam1 using the "Shift and Add" approach described in the text. Representative vertical and horizonal Line Scan Functions (LSFs) are shown, revealing an average FWHM of the PSF of 1.30 pixels. (bottom four) Estimated PSF for TTCam2 using the "Shift and Add" approach described in the text. The graphs, image, and data in Table 6 show that TTCam2 has a broader and more skewed PSF than TTCam1, with an average FWHM of the PSF of 1.44 pixels.

Table 6. TTCam Normalized Point Spread Functions (PSF)

TTCam1 PSF Central 7x7 Pixels, Normalized							
	-3	*-2*	*-1*	*0*	*1*	*2*	*3*
-3	0.001	0.001	0.002	0.003	0.002	0.001	0.001
-2	0.001	0.003	0.007	0.010	0.007	0.003	0.001
-1	0.002	0.006	0.030	0.084	0.030	0.008	0.003
0	0.002	0.009	0.088	**0.370**	0.090	0.020	0.005
1	0.002	0.006	0.027	0.084	0.031	0.009	0.003
2	0.001	0.003	0.007	0.012	0.008	0.003	0.002
3	0.001	0.001	0.002	0.003	0.002	0.001	0.001
TTCam2 PSF Central 7x7 Pixels, Normalized							
	-3	*-2*	*-1*	*0*	*1*	*2*	*3*
-3	0.004	0.005	0.007	0.006	0.003	0.001	0.001
-2	0.007	0.014	0.022	0.021	0.007	0.002	0.001
-1	0.010	0.026	0.063	0.085	0.021	0.004	0.001
0	0.009	0.030	0.102	**0.271**	0.070	0.011	0.002
1	0.006	0.015	0.036	0.072	0.030	0.005	0.002
2	0.002	0.004	0.005	0.006	0.003	0.001	0.001
3	0.001	0.001	0.001	0.001	0.001	0.001	0.001

$$S = \begin{bmatrix} \frac{1}{\sigma_x^2} & 0 \\ 0 & \frac{1}{\sigma_y^2} \end{bmatrix}$$

A is the amplitude of the PSF, (x_0, y_0) is the center of the PSF, θ is the angle between the image X-axis and the principal axis of the Gaussian, σ_x is the Gaussian RMS width in the semi-major axis direction, and σ_y is the Gaussian RMS width in the semi-minor axis direction.

This Gaussian function was fit to the PSFs of 4361 stars in TTCam1 images and 2684 stars in TTCam2 images to evaluate and characterize the PSF of the two imagers. Only stars with a peak signal between 500 and 3500 DN were selected to avoid stars with a low signal-to-noise ratio as well as saturated stars. For TTCam1, the mean semi-major axis width was 0.599 ± 0.064 pixels and the mean semi-minor axis width was 0.507 ± 0.063 pixels. The rotation angles seemed mostly random for TTCam1 but most star PSFs had rotation angles between 90° and 180°, as seen in Figure 14. For TTCam2, the mean semi-major axis width was 0.757 ± 0.166 pixels and the mean semi-minor axis width was 0.574 ± 0.128 pixels. Most TTCam2 star PSFs had rotation angles between roughly 120° and 170°, as seen in Figure 14.

5 Conclusions

This paper details the pre-flight and in-flight calibration of the Lucy mission's TTCam instruments, in support of eventual scientific observations of the Trojan asteroids during flyby encounters. We find that both sensors exhibit excellent linearity (with a maximum deviation from fit $< 2.2\%$), low read noise ($< 15\ e^-$), no statistically significant dark current at the expected operational temperatures, and uniform pixel-to-pixel responsivity variations of $< 1\%$. In-flight observations provide additional confirmation of instrument performance and characteristics, including: (1) Observations of star fields that confirm extremely little geometric distortion across the field of view; (2) Observations of the Earth and Moon that validate pre-flight expectations of the responsivity of the

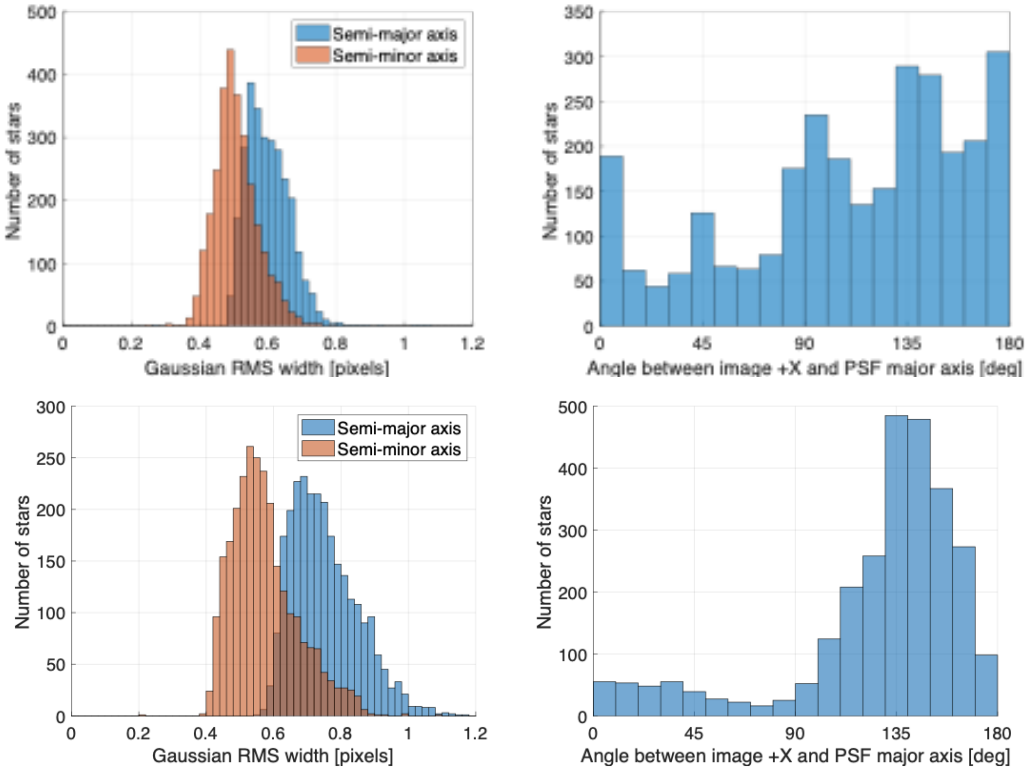

Figure 14. (top) Histograms of the fitted Gaussian widths (left) and rotation angles (right) for 4361 stars in TTCam1 images. (bottom) Histograms of the fitted Gaussian widths (left) and rotation angles (right) for 4361 stars in TTCam1 images.

cameras within a correlation coefficient of r=0.95; and (3) Observations of scattered sunlight at the viewing geometries of the eventual asteroid encounters that show that scattered light levels should be insignificant compared to signal from the targets.

We have used the pre-flight and in-flight calibration information to develop an exposure time model as well as a calibration pipeline that converts each raw TTCam image to calibrated radiance and radiance factor, including associated uncertainty images for those derived parameters and a bad pixel image that flags any saturated or nonlinear pixels. We present details on the ancillary input files and parameters needed to run the pipeline, as well as the output FITS format calibrated data files and their associated ancillary data. Additional information on the measurement requirements, design, and expected scientific results from the TTCam instruments is provided in a companion paper by Bell et al. (2023).

6 Open Research

All calibration data from pre-calibration activities, as well as ancillary calibration files such as flat fields and bad pixel maps, are available at the ASU Library Research Data Repository, at https://doi.org/10.48349/ASU/RVHF83 (Bell & Zhao, 2023). All in-flight data taken with the TTCams used for validation of the calibration pipeline are or will soon be archived in the NASA Planetary Data System for full public dissemination.

Appendix A TTCam Predicted Pre-flight Optical Specifications

Table A1. Lucy Mission Terminal Tracking Cameras: Pre-flight Optical Specifications

Focal length	29.7 mm (all-refractive; fixed focus)
Focal ratio	f/2.95
Depth of Field	≈200 m to ∞ (hyperfocal: 133.7 m; near-focus: 66.8 m)
entrance pupil aperture	9.9 mm
aperture area	77 mm^2
exit pupil diameter	7.1 mm
t/#	< 3.36
pixel solid angle	5.5×10^{-9} sr
throughput ($A_0\Omega$)	4.22×10^{-7} mm^2 sr
IFOV	74.1 μrad/pixel (74.1 m/pixel @ 1000 km)
FOV	11.0° × 8.2° (13.7° diagonal) (193 × 143 km @ 1000 km)
Filters	1
Filter bandpass	Panchromatic: 425-675 nm
Effective Wavelength	Avg. Red Trojan: 548.6 nm; Avg. Less-Red Trojan: 545.5 nm
Optics Transmission	$> 80\%$
Optics Distortion	0.12% average in corners of field of view
MTF	0.19 (optics+filter+sensor) at Nyquist = 227 l.p./mm

Appendix B Lucy TTCam Default Square-Root Companding (12 to 8 bit DN) "Mode 17" Lookup Table

Original Raw 12-bit range	Downlinked 8-bit DN	12-bit	8-bit	12-bit	8-bit	12-bit	8-bit	12-bit	8-bit	12-bit	8-bit	12-bit	8-bit	12-bit	8-bit
0	0	**69-73**	32	**265-272**	64	**587-598**	96	**1035-1050**	128	**1611-1630**	160	**2313-2336**	192	**3141-3168**	224
1	1	**74-77**	33	**273-280**	65	**599-610**	97	**1051-1066**	129	**1631-1650**	161	**2337-2360**	193	**3169-3197**	225
2	2	**78-81**	34	**281-288**	66	**611-622**	98	**1067-1083**	130	**1651-1670**	162	**2361-2384**	194	**3198-3225**	226
3	3	**82-86**	35	**289-297**	67	**623-635**	99	**1084-1099**	131	**1671-1690**	163	**2385-2408**	195	**3226-3253**	227
4	4	**87-91**	36	**298-306**	68	**636-647**	100	**1100-1116**	132	**1691-1711**	164	**2409-2433**	196	**3254-3281**	228
5	5	**92-95**	37	**307-314**	69	**648-660**	101	**1117-1132**	133	**1712-1732**	165	**2434-2457**	197	**3282-3310**	229
6	6	**96-100**	38	**315-323**	70	**661-673**	102	**1133-1149**	134	**1733-1752**	166	**2458-2482**	198	**3311-3339**	230
7	7	**101-105**	39	**324-332**	71	**674-686**	103	**1150-1166**	135	**1753-1773**	167	**2483-2507**	199	**3340-3368**	231
8	8	**106-111**	40	**333-341**	72	**687-699**	104	**1167-1183**	136	**1774-1794**	168	**2508-2532**	200	**3369-3396**	232
9	9	**112-116**	41	**342-351**	73	**700-712**	105	**1184-1200**	137	**1795-1815**	169	**2533-2557**	201	**3397-3426**	233
10	10	**117-121**	42	**352-360**	74	**713-725**	106	**1201-1218**	138	**1816-1837**	170	**2558-2582**	202	**3427-3455**	234
11	11	**122-127**	43	**361-370**	75	**726-739**	107	**1219-1235**	139	**1838-1858**	171	**2583-2608**	203	**3456-3484**	235
12-13	12	**128-133**	44	**371-379**	76	**740-752**	108	**1236-1253**	140	**1859-1879**	172	**2609-2633**	204	**3485-3513**	236
14-14	13	**134-138**	45	**380-389**	77	**753-766**	109	**1254-1270**	141	**1880-1901**	173	**2634-2659**	205	**3514-3543**	237
15-16	14	**139-144**	46	**390-399**	78	**767-780**	110	**1271-1288**	142	**1902-1923**	174	**2660-2684**	206	**3544-3573**	238
17-18	15	**145-150**	47	**400-409**	79	**781-794**	111	**1289-1306**	143	**1924-1945**	175	**2685-2710**	207	**3574-3602**	239
19-21	16	**151-156**	48	**410-419**	80	**795-808**	112	**1307-1324**	144	**1946-1967**	176	**2711-2736**	208	**3603-3632**	240
22-23	17	**157-163**	49	**420-429**	81	**809-822**	113	**1325-1342**	145	**1968-1989**	177	**2737-2762**	209	**3633-3662**	241
24-25	18	**164-169**	50	**430-439**	82	**823-837**	114	**1343-1360**	146	**1990-2011**	178	**2763-2789**	210	**3663-3693**	242
26-28	19	**170-176**	51	**440-450**	83	**838-851**	115	**1361-1379**	147	**2012-2034**	179	**2790-2815**	211	**3694-3723**	243
29-31	20	**177-182**	52	**451-461**	84	**852-866**	116	**1380-1397**	148	**2035-2056**	180	**2816-2841**	212	**3724-3753**	244
32-34	21	**183-189**	53	**462-471**	85	**867-880**	117	**1398-1416**	149	**2057-2079**	181	**2842-2868**	213	**3754-3784**	245
35-36	22	**190-196**	54	**472-482**	86	**881-895**	118	**1417-1435**	150	**2080-2101**	182	**2869-2895**	214	**3785-3814**	246
37-40	23	**197-203**	55	**483-493**	87	**896-910**	119	**1436-1454**	151	**2102-2124**	183	**2896-2921**	215	**3815-3845**	247
41-43	24	**204-210**	56	**494-504**	88	**911-925**	120	**1455-1473**	152	**2125-2147**	184	**2922-2948**	216	**3846-3876**	248
44-46	25	**211-217**	57	**505-516**	89	**926-940**	121	**1474-1492**	153	**2148-2170**	185	**2949-2975**	217	**3877-3907**	249
47-49	26	**218-225**	58	**517-527**	90	**941-956**	122	**1493-1511**	154	**2171-2194**	186	**2976-3003**	218	**3908-3938**	250
50-53	27	**226-232**	59	**528-538**	91	**957-971**	123	**1512-1531**	155	**2195-2217**	187	**3004-3030**	219	**3939-3970**	251
54-57	28	**233-240**	60	**539-550**	92	**972-987**	124	**1532-1550**	156	**2218-2240**	188	**3031-3057**	220	**3971-4001**	252
58-61	29	**241-248**	61	**551-562**	93	**988-1002**	125	**1551-1570**	157	**2241-2264**	189	**3058-3085**	221	**4002-4033**	253
62-64	30	**249-256**	62	**563-573**	94	**1003-1018**	126	**1571-1590**	158	**2265-2288**	190	**3086-3113**	222	**4034-4064**	254
65-68	31	**257-264**	63	**574-586**	95	**1019-1034**	127	**1591-1610**	159	**2289-2312**	191	**3114-3140**	223	**4065-4095**	255

Appendix C Lucy TTCam Default Square-Root Decompanding (8 to 12 bit DN) "Mode 17" Lookup Table

8-bit	12-bit	8-bit	12-bit	8-bit	12-bit	8-bit	12-bit	8-bit	12-bit	8-bit	12-bit	8-bit	12-bit	8-bit	12-bit
0	0	**32**	71	**64**	268	**96**	592	**128**	1042	**160**	1620	**192**	2324	**224**	3154
1	1	**33**	75	**65**	276	**97**	604	**129**	1058	**161**	1640	**193**	2348	**225**	3183
2	2	**34**	79	**66**	284	**98**	616	**130**	1075	**162**	1660	**194**	2372	**226**	3211
3	3	**35**	84	**67**	293	**99**	629	**131**	1091	**163**	1680	**195**	2396	**227**	3239
4	4	**36**	89	**68**	302	**100**	641	**132**	1108	**164**	1701	**196**	2421	**228**	3267
5	5	**37**	93	**69**	310	**101**	654	**133**	1124	**165**	1722	**197**	2445	**229**	3296
6	6	**38**	98	**70**	319	**102**	667	**134**	1141	**166**	1742	**198**	2470	**230**	3325
7	7	**39**	103	**71**	328	**103**	680	**135**	1158	**167**	1763	**199**	2495	**231**	3354
8	8	**40**	108	**72**	337	**104**	693	**136**	1175	**168**	1784	**200**	2520	**232**	3382
9	9	**41**	114	**73**	346	**105**	706	**137**	1192	**169**	1805	**201**	2545	**233**	3411
10	10	**42**	119	**74**	356	**106**	719	**138**	1209	**170**	1826	**202**	2570	**234**	3441
11	11	**43**	124	**75**	365	**107**	732	**139**	1227	**171**	1848	**203**	2595	**235**	3470
12	12	**44**	130	**76**	375	**108**	746	**140**	1244	**172**	1869	**204**	2621	**236**	3499
13	14	**45**	136	**77**	384	**109**	759	**141**	1262	**173**	1890	**205**	2646	**237**	3528
14	15	**46**	141	**78**	394	**110**	773	**142**	1279	**174**	1912	**206**	2672	**238**	3558
15	17	**47**	147	**79**	404	**111**	787	**143**	1297	**175**	1934	**207**	2697	**239**	3588
16	20	**48**	153	**80**	414	**112**	801	**144**	1315	**176**	1956	**208**	2723	**240**	3617
17	22	**49**	160	**81**	424	**113**	815	**145**	1333	**177**	1978	**209**	2749	**241**	3647
18	24	**50**	166	**82**	434	**114**	830	**146**	1351	**178**	2000	**210**	2776	**242**	3678
19	27	**51**	173	**83**	445	**115**	844	**147**	1370	**179**	2023	**211**	2802	**243**	3708
20	30	**52**	179	**84**	456	**116**	859	**148**	1388	**180**	2045	**212**	2828	**244**	3738
21	33	**53**	186	**85**	466	**117**	873	**149**	1407	**181**	2068	**213**	2855	**245**	3769
22	35	**54**	193	**86**	477	**118**	888	**150**	1426	**182**	2090	**214**	2882	**246**	3799
23	38	**55**	200	**87**	488	**119**	903	**151**	1445	**183**	2113	**215**	2908	**247**	3830
24	42	**56**	207	**88**	499	**120**	918	**152**	1464	**184**	2136	**216**	2935	**248**	3861
25	45	**57**	214	**89**	510	**121**	933	**153**	1483	**185**	2159	**217**	2962	**249**	3892
26	48	**58**	221	**90**	522	**122**	948	**154**	1502	**186**	2182	**218**	2989	**250**	3923
27	51	**59**	229	**91**	533	**123**	964	**155**	1521	**187**	2206	**219**	3017	**251**	3954
28	55	**60**	236	**92**	544	**124**	979	**156**	1541	**188**	2229	**220**	3044	**252**	3986
29	59	**61**	244	**93**	556	**125**	995	**157**	1560	**189**	2252	**221**	3071	**253**	4017
30	63	**62**	252	**94**	568	**126**	1010	**158**	1580	**190**	2276	**222**	3099	**254**	4049
31	66	**63**	260	**95**	580	**127**	1026	**159**	1600	**191**	2300	**223**	3127	**255**	4080

Acknowledgments

We would like to thank all the members of the Lucy mission team, including the MSSS staff, the Lockheed Martin support staff, NASA support staff, and the subcontractors and vendors, who supported the Lucy mission through unpredictable hardships, including a global pandemic. In addition, we would like to thank Danielle Smilovsky and Oketa Basha at Arizona State University for their work on the TTCam calibration pipeline and in-flight star observations, respectively. The work performed here by researchers at Arizona State University was supported by the NASA Lucy mission, via subcontract #K99056JRG from the Southwest Research Institute.

References

Acton, C. H. (1996). Ancillary data services of nasa's navigation and ancillary information facility. *Planetary and Space Science*, *44*, 65-70.

Anderson, J. (2016, March). *Empirical Models for the WFC3/IR PSF.* Instrument Science Report WFC3 2016-12, 42 pages.

Anderson, J., & King, I. R. (2000, October). Toward High-Precision Astrometry with WFPC2. I. Deriving an Accurate Point-Spread Function. *PASP*, *112*(776), 1360-1382. doi: 10.1086/316632

Bell, J., Godber, A., McNair, S., Caplinger, M., Maki, J., Lemmon, M., ... Deen, R. (2017, July 2). The mars science laboratory curiosity rover mastcam instruments: Preflight and in-flight calibration, validation, and data archiving. *Earth and Space Science*, *4*(7), 396–452. doi: 10.1002/2016EA000219

Bell, J., & Zhao, A. (2023). *Lucy Terminal Tracking Camera (TTCam) Pre-flight Calibration Data* [dataset]. ASU Library Research Data Repository. Retrieved from `https://doi.org/10.48349/ASU/RVHF83` doi: 10.48349/ASU/RVHF83

Bell, J., Zhao, Y., Cisneros, E., Beasley, M., Olkin, C., Caplinger, M. A., ... Bos, B. J. (2023). The terminal tracking camera system on the nasa lucy trojan asteroid discovery mission. *Space Science Reviews*.

Bos, B., Nelson, D., Pelgrift, J., Liounis, A., Doelling, D., Norman, C., ... Lauretta, D. (2020, 06). In-flight calibration and performance of the osiris-rex touch and go camera system (tagcams). *Space Science Reviews*, *216*. doi: 10.1007/s11214-020-00682-x

Bradley, L., Sipőcz, B., Robitaille, T., Tollerud, E., Vinícius, Z., Deil, C., ... Souchereau, H. (2023, May). *astropy/photutils: 1.8.0.* Zenodo. Retrieved from `https://doi.org/10.5281/zenodo.7946442` doi: 10.5281/zenodo.7946442

Good, P., Faiks, P., & Pisano, W. (2022). *Terminal tracking for the lucy trojan asteroid mission.* Retrieved from `https://ntrs.nasa.gov/api/citations/20220001851/downloads/AAS-22-131TerminalTrackingfortheLucyTrojanAsteroidMission.pdf` (44th Annual AAS Guidance, Navigation and Control Conference (Breckenridge, CO), Paper AAS 22-131)

Hapke, B. (2012). *Theory of reflectance and emittance spectroscopy* (2nd ed.). Cambridge University Press. doi: 10.1017/CBO9781139025683

Janesick, J., Klaasen, K. P., & Elliott, T. S. (1987). Charge-coupled-device charge-collection efficiency and the photon-transfer technique. *Optical Engineering*, *26*, 972-980.

Levison, H. F., Olkin, C. B., Noll, K. S., Marchi, S., Bell III, J. F., Bierhaus, E., ... others (2021). Lucy mission to the trojan asteroids: Science goals. *The Planetary Science Journal*, *2*(5), 171.

Malin, M. C., Edgett, K., Jensen, E., & Lipkaman, L. (2013, October 29). Mars science laboratory project software interface specification (sis): Mast camera (mastcam), mars hand lens imager (mahli), and mars descent imager (mardi) experiment data record (edr), reduced data record (rdr), and pds data products. *JPL D-75410*. Retrieved from `http://pds-imaging.jpl.nasa.gov/`

`data/msl/MSLMST_0001/DOCUMENT/MSL_MMM_EDR_RDR_DPSIS.PDF`

Olkin, C. B., Levison, H. F., Vincent, M., Noll, K. S., Andrews, J., Gray, S., ... others (2021). Lucy mission to the trojan asteroids: instrumentation and encounter concept of operations. *The Planetary Science Journal*, *2*(5), 172.

OpenCV. (2014). *Camera calibration and 3d reconstruction* [software].

Sato, H., Robinson, M., Hapke, B., Denevi, B., & Boyd, A. (2014, 08). Resolved hapke parameter maps of the moon. *Journal of Geophysical Research: Planets*, *119*. doi: 10.1002/2013JE004580

Spencer, J. R., Bell III, J. F., Christensen, P. R., Dello Russo, N., Kaplan, H. H., Reuter, D. C., ... Weaver, H. A. (2024). The first lucy earth flyby (ega1). *Space Sci. Rev.*, *220*(3). doi: 10.1007/s11214023-01034-1